

# Flux calibration of broad-band far-infrared and submillimetre photometric instruments: theory and application to *Herschel*-SPIRE

M. J. Griffin,<sup>1\*</sup> C. E. North,<sup>1\*</sup> B. Schulz,<sup>2,3</sup> A. Amaral-Rogers,<sup>1</sup> G. Bendo,<sup>4</sup> J. Bock,<sup>2,5</sup> L. Conversi,<sup>6</sup> A. Conley,<sup>7</sup> C. D. Dowell,<sup>5</sup> M. Ferlet,<sup>8</sup> J. Glenn,<sup>7</sup> T. Lim,<sup>8</sup> C. Pearson,<sup>8,9</sup> M. Pohlen,<sup>10</sup> B. Sibthorpe,<sup>11</sup> L. Spencer,<sup>1</sup> B. Swinyard<sup>8,12</sup> and I. Valtchanov<sup>6</sup>

<sup>1</sup>*School of Physics & Astronomy, Cardiff University, The Parade, Cardiff CF24 3AA, UK*

<sup>2</sup>*California Institute of Technology, 1200 E. California Blvd., Pasadena, CA 91125, USA*

<sup>3</sup>*Infrared Processing and Analysis Center, MS 100-22, California Institute of Technology, JPL, Pasadena, CA 91125, USA*

<sup>4</sup>*Jodrell Bank Centre for Astrophysics, University of Manchester, Alan Turing Building, Manchester M13 9PL, UK*

<sup>5</sup>*Jet Propulsion Laboratory, 4800 Oak Grove Drive, Pasadena, CA 91109, USA*

<sup>6</sup>*Herschel Science Centre, European Space Astronomy Centre, ESA, Villanueva de la Cañada, E-28691 Madrid, Spain*

<sup>7</sup>*Center for Astrophysics and Space Astronomy, CB-389, University of Colorado, Boulder, CO 80309, USA*

<sup>8</sup>*RAL Space, Science and Technology Facilities Council, Rutherford Appleton Laboratory, Harwell Oxford, Didcot, Oxfordshire OX11 0QX, UK*

<sup>9</sup>*Department of Physical Science, The Open University, Milton Keynes MK7 6AA, UK*

<sup>10</sup>*Gemini Observatory Northern Operations Center, 670 N. A'ohoku Place, Hilo, HI 96720, USA*

<sup>11</sup>*SRON Netherlands Institute for Space Research, Landleven 12, NL-9747 AD Groningen, the Netherlands*

<sup>12</sup>*Department of Physics & Astronomy, University College London, Gower Place, London WC1E 6BT, UK*

Accepted 2013 June 5. Received 2013 May 21; in original form 2013 February 8

## ABSTRACT

Photometric instruments operating at far-infrared to millimetre wavelengths often have broad spectral passbands ( $\lambda/\Delta\lambda \sim 3$  or less), especially those operating in space. A broad passband can result in significant variation of the beam profile and aperture efficiency across the passband, effects which thus far have not generally been taken into account in the flux calibration of such instruments. With absolute calibration uncertainties associated with the brightness of primary calibration standards now in the region of 5 per cent or less, variation of the beam properties across the passband can be a significant contributor to the overall calibration accuracy for extended emission. We present a calibration framework which takes such variations into account for both antenna-coupled and absorber-coupled focal plane architectures. The scheme covers point source and extended source cases, and also the intermediate case of a semi-extended source profile. We apply the new method to the Spectral and Photometric Imaging Receiver (SPIRE) photometer on board the *Herschel* Space Observatory.

**Key words:** instrumentation: photometers – methods: observational – techniques: photometric – submillimetre: general.

## 1 INTRODUCTION

Broad-band bolometric detector arrays are used in sensitive photometric instruments for far-infrared (FIR) and submillimetre astronomy, particularly in space-borne instruments for which there are no atmospheric limitations on the width of the accepted passband. Considerations of photometric sensitivity and optimum spectral definition lead to the use of spectral passbands with resolution  $\lambda/\Delta\lambda \sim 2$ –3. For such instruments, achieving the most accurate calibration may require taking into account the variation of the beam profile and aperture efficiency across the passband. Recent and forthcoming examples include the *Herschel*-SPIRE (Griffin et al.

2010), *Herschel*-PACS (Poglitsch et al. 2010) and *Planck*-HFI (Ade et al. 2010) satellite instruments, balloon-borne instruments such as BLAST (Pascale et al. 2008), PILOT (Bernard et al. 2010) and EBEX (Reichborn-Kjennerud et al. 2010), and the proposed next-generation CMB polarization satellite mission, CORE (Armitage-Caplan et al. 2011). Ground-based instruments such as Submillimetre Common-User Bolometer Array (SCUBA; Holland et al. 1999) and SCUBA-2 (Holland et al. 2006), BOLOCAM (Glenn et al. 2003), LABOCA (Siringo et al. 2009), SABOCA (Siringo et al. 2010), ACBAR (Runyan et al. 2003), usually have narrow passbands ( $\lambda/\Delta\lambda = 5$ –10) dictated by the widths of the atmospheric windows in which they observe, although antenna-coupled instruments operating at low frequency at high-transparency sites, such as the South Pole Telescope, can have  $\lambda/\Delta\lambda$  as low as  $\sim 4$  (Ruhl et al. 2004).

\*E-mail: Matt.Griffin@astro.cf.ac.uk (MJG); chris.north@astro.cf.ac.uk (CEN)

Flux calibration in the FIR and submillimetre is normally based on use of the planets Mars, Uranus or Neptune as the primary standards (e.g. Griffin & Orton 1993). The absolute uncertainty in planetary models is now at the level of 5 per cent (e.g. Moreno 1998, 2012), and the stability and data quality achievable, particularly with space-borne instruments, means that relative calibration uncertainties can be less than this. These improvements in the absolute knowledge of the primary standards and in data quality mean that care needs to be taken in all aspects of flux calibration to avoid systematic errors dominating the final results. For broad-band photometry, accurate knowledge of the instrument relative spectral response function (SRF) is essential, as significant colour corrections must be applied to account for differences in the spectral energy distributions (SEDs) of the calibrator and the science target. The calibration of extended emission using a point-like flux standard also requires good knowledge of the beam properties. Close attention may also be needed to eliminate the effects of non-linearity in the detector response. Normally, the conversion from point source to extended source calibration is effected using an accurate estimation of the beam solid angle as measured using a high signal-to-noise map of a bright point-like source. A complication, which has not yet been addressed, is that for broad-band detectors, the beam width varies significantly across the passband. The measured beam solid angle represents an average value across the band, and also depends on the spectral shape of the object used to map the beam. It is therefore not exactly the correct solid angle to use when observing emission with a different spectral index (which is usually the case). Depending on the bandwidth and the overall error budget, the variation of the beam profile across the passband may or may not need to be taken into account in the calibration procedure.

In this paper, we outline an approach to flux calibration suitable for point and extended sources, and use as an example the *Herschel*-SPIRE camera, which observes in three photometric bands centred near 250, 350 and 500  $\mu\text{m}$ , and for which Neptune is used as the primary flux standard. Detector non-linearity correction and many other practical issues involved in making accurate comparative measurements of the signal levels from the calibrator and the source are not the subject of this paper and will not be further discussed here. Such aspects will be addressed for the case of SPIRE in Bendo et al. (2013) and Lim et al. (in preparation).

In Section 2, the method adopted for point source calibration is outlined and the formulae appropriate for the derivation of a well-defined monochromatic flux density and for appropriate colour correction are derived. Section 3 outlines a scheme for the accurate calibration of extended or semi-extended emission, which in principle requires knowledge of both the beam properties of the system as a function of wavelength within the spectral passband, and of the spatial distribution of the source brightness. In Section 4, we consider the manner in which the aperture efficiency and beam profile vary across the passband for both a single-moded feedhorn antenna-coupled detector and an absorber-coupled detector, and in Section 5, we present results for the cases of ideal flat-topped passband of widths  $\lambda/\Delta\lambda = 3, 5$  and 10. The application of this methodology to *Herschel*-SPIRE calibration is described and discussed in Section 6. Conclusions are summarized in Section 7, and Appendix A contains a list of symbols used in the paper.

## 2 CALIBRATION OF ON-AXIS POINT SOURCE OBSERVATIONS

Consider an instrument with an SRF defined by  $F(\nu)$ , i.e. the instrument transmission as a function of frequency,  $\nu$  with arbitrary

normalization. Let  $\eta(\nu)$  be the aperture efficiency, defined as the fraction of the total power from an on-axis point source that is coupled to the detector. Consider an on-axis observation of a point source with spectral flux density  $S(\nu)$  at the telescope aperture. The source power absorbed by the detector is directly proportional to the integral over the passband of the flux density weighted by the product of  $F(\nu)$  and  $\eta(\nu)$ . Assuming that the detector signal is, or can be linearized so as to be, directly proportional to the absorbed power, the property of the source that is measured, is the SRF-weighted flux density, given by

$$\bar{S}_{\text{Meas}} = \frac{\int_{\nu} S(\nu)F(\nu)\eta(\nu) d\nu}{\int_{\nu} F(\nu)\eta(\nu) d\nu}. \quad (1)$$

When observing a point-like calibrator, the quantity that is directly proportional to absorbed detector power is the calibrator SRF-weighted flux density, given by

$$\bar{S}_{\text{C}} = K_{\text{Beam}}(\theta_{\text{p}}, \theta_{\text{Beam}}) \left[ \frac{\int_{\nu} S_{\text{C}}(\nu)F(\nu)\eta(\nu) d\nu}{\int_{\nu} F(\nu)\eta(\nu) d\nu} \right], \quad (2)$$

where  $S_{\text{C}}(\nu)$  represents the calibrator spectrum and  $K_{\text{Beam}}(\theta_{\text{p}}, \theta_{\text{Beam}})$  is a correction factor for possible partial resolution of the calibrator by the telescope beam. For a Gaussian main beam profile coupling to a uniformly bright disc (such as planet or asteroid), the beam-correction factor is given by (Ulich & Haas 1976)

$$K_{\text{Beam}}(\theta_{\text{p}}, \theta_{\text{Beam}}) = \frac{1 - \exp\left(-\frac{4 \ln(2)\theta_{\text{p}}^2}{\theta_{\text{Beam}}^2}\right)}{\frac{4 \ln(2)\theta_{\text{p}}^2}{\theta_{\text{Beam}}^2}}, \quad (3)$$

where  $\theta_{\text{p}}$  is the angular radius of the disc, and  $\theta_{\text{Beam}}$  is the beam full-width half-maximum (FWHM) value. Because both the beam width and  $\theta_{\text{p}}$  can vary across the passband,  $K_{\text{Beam}}$  can have a weak dependence on frequency.

The calibration flux density,  $S_{\text{C}}$ , can thus be derived from a knowledge of the calibrator spectrum and angular size, as well as the instrument SRF and aperture efficiency functions. It is convenient and conventional to quote the result of a photometric measurement in the form of a monochromatic flux density at a suitable standard frequency,  $\nu_0$ , near the centre of the passband. If an unknown source has the same spectral shape as the calibrator, then its flux density at any frequency can be determined simply from the ratio of the measured signals multiplied by the calibrator flux density at that frequency. In the more usual case in which the source and calibrator have different spectral shapes, the definition of a monochromatic flux density requires, in addition to a standard frequency, some assumption about the shape of the source spectrum.

For an operating instrument, it is convenient to implement a standard automatic pipeline which processes the observational data to produce corresponding flux densities based on some default assumption concerning the source spectrum:

$$S(\nu) = S(\nu_0)f(\nu, \nu_0), \quad (4)$$

where  $f(\nu, \nu_0)$  characterizes the shape of the spectrum. Commonly adopted assumptions for the spectral shape are a power law with some spectral index,  $\alpha$ :

$$f(\alpha, \nu, \nu_0) = \left(\frac{\nu}{\nu_0}\right)^{\alpha}, \quad (5)$$

or a modified blackbody characterized by a blackbody spectrum  $\mathcal{B}(\nu, T)$  for temperature  $T$ , modified by an emissivity that varies

with frequency according to a power law with index  $\beta$ :

$$f(T, \beta, \nu, \nu_0) = \frac{\mathcal{B}(\nu, T)}{\mathcal{B}(\nu_0, T)} \left( \frac{\nu}{\nu_0} \right)^\beta$$

$$= \frac{\exp\left(\frac{h\nu_0}{k_B T}\right) - 1}{\exp\left(\frac{h\nu}{k_B T}\right) - 1} \left( \frac{\nu}{\nu_0} \right)^{3+\beta}, \quad (6)$$

where  $h$  is the Planck constant and  $k_B$  is the Boltzmann constant. The power-law spectrum in equation (5) is simple to estimate based on empirical data from two or more photometric measurements, while the modified blackbody spectrum in equation (6) is a simple model representing optically thin thermal dust emission.

From equations (1) and (4), and assuming the case of a source with a power-law SED given by  $f(\alpha, \nu, \nu_0)$  as in equation (5), the monochromatic source flux density at frequency  $\nu_0$  is given by

$$S(\nu_0) = K_{\text{MonP}}(f, \nu_0) \cdot \bar{S}_{\text{Meas}}, \quad (7)$$

with

$$K_{\text{MonP}}(\alpha, \nu_0) = \frac{\int_\nu F(\nu)\eta(\nu) d\nu}{\int_\nu \left(\frac{\nu}{\nu_0}\right)^\alpha F(\nu)\eta(\nu) d\nu}, \quad (8)$$

while for a modified blackbody spectrum,  $K_{\text{MonP}}$  is a function of  $(T, \beta, \nu_0)$  instead of  $(\alpha, \nu_0)$ .

To derive the monochromatic flux density at frequency  $\nu_0$ , the measured SRF-weighted flux density of a point source is therefore multiplied by  $K_{\text{MonP}}$ , which can be computed from the known properties of the instrument and an assumed source spectral shape. In pipeline processing of instrument data, a power-law spectrum with a standard value of  $\alpha_0 = -1$  is often adopted, corresponding to a source spectrum which is flat in  $\nu S(\nu)$ , i.e. with frequency-independent power flux. This is the convention used in the generation of pipeline flux densities for many previous instruments in the mid-infrared through millimetre, including *COBE/DIRBE* (Hauser et al. 1998), *IRAS* (Beichman et al. 1988), *ISOCAM* (Cesarsky et al. 1996), *ISOPHOT* (Lemke et al. 1996), and for the *Herschel* photometers *PACS* (Poglitsch et al. 2010) and *SPIRE* (Swinyard et al. 2010). An exception is *Spitzer-MIPS*, which uses a  $10^4$  K blackbody as a reference spectrum (Stansberry et al. 2007). This assumption results in a pipeline flux density

$$S_{\text{Pip}}(\alpha_0, \nu_0) = K_{\text{MonP}}(\alpha_0, \nu_0) \cdot \bar{S}_{\text{Meas}}. \quad (9)$$

The assumption that the source has a power-law spectrum with a spectral index  $\alpha_0$  will not be valid in most cases, requiring the application of a point source colour-correction factor,  $K_{\text{ColP}}$ , based on the best available information on the actual source spectrum (for instance, measurements at multiple wavelengths). The true monochromatic flux density is then estimated as

$$S(\nu_0) = K_{\text{ColP}}(f, \alpha_0, \nu_0) \cdot S_{\text{Pip}}(\nu_0). \quad (10)$$

For an assumed power-law spectrum, with  $f(\alpha, \nu, \nu_0)$  as given in equation (5),

$$K_{\text{ColP}}(\alpha, \alpha_0, \nu_0) = \frac{K_{\text{MonP}}(\alpha, \nu_0)}{K_{\text{MonP}}(\alpha_0, \nu_0)}$$

$$= \left[ \frac{\int_\nu F(\nu)\eta(\nu)\nu^{\alpha_0} d\nu}{\int_\nu F(\nu)\eta(\nu)\nu^\alpha d\nu} \right] \nu_0^{\alpha-\alpha_0}. \quad (11)$$

In the case of an assumed modified blackbody spectrum, with  $f(T, \beta, \nu, \nu_0)$  as given in equation (6),

$$K_{\text{ColP}}(T, \beta, \alpha_0, \nu_0) = \frac{\nu_0^{3+\beta-\alpha_0}}{e^{h\nu_0/k_B T} - 1}$$

$$\times \left[ \frac{\int_\nu \nu^{\alpha_0} F(\nu)\eta(\nu) d\nu}{\int_\nu \left(\frac{\nu^{\alpha_0}}{e^{h\nu/k_B T} - 1}\right) F(\nu)\eta(\nu) d\nu} \right]. \quad (12)$$

If  $h\nu \ll k_B T$  (i.e. a modified blackbody in the Rayleigh–Jeans regime), this is equivalent to the power-law case with  $\alpha = \beta + 2$ .

### 3 CALIBRATION OF EXTENDED EMISSION

A conventional approach to the calibration of extended emission is to divide the measured flux densities (based on a point source calibration scheme) by the solid angle of the beam to convert a map from units of flux density (Jy in beam) to units of surface brightness (e.g. Jy pixel<sup>-1</sup> or Jy sr<sup>-1</sup>). This procedure is potentially inaccurate if the beam profile varies as a function of frequency within the band, in which case it is not valid to define a particular beam area. As discussed in Section 4 below, in the case of broad-band photometric observations the beam can vary significantly across the passband. To account correctly for the wavelength dependence of the beam, it is then necessary to include it explicitly in the integral for the measured flux density.

Consider a point source observation in which the source is not on axis, but at some angular position with respect to the axis, defined by orthogonal offset angles  $\theta$  and  $\phi$ . Let the frequency-dependent normalized beam response as a function of position be  $B(\nu, \theta, \phi)$ , so that at a given frequency,  $\nu$ , the response to the source at position  $(\theta, \phi)$  is reduced by that factor with respect to the on-axis value at that frequency. A slightly extended source at  $(\theta, \phi)$ , with surface brightness  $I(\nu, \theta, \phi)$  and angular extent  $(d\theta, d\phi)$ , will therefore lead to a measured flux density given by

$$d\bar{S}_{\text{Meas}}(\theta, \phi) = \frac{\int_\nu I(\nu, \theta, \phi) B(\nu, \theta, \phi) d\theta d\phi F(\nu)\eta(\nu) d\nu}{\int_\nu F(\nu)\eta(\nu) d\nu}. \quad (13)$$

The total measured flux density within the entire beam for an extended source is then

$$\bar{S}_{\text{Meas}} = \frac{\int_\nu y(\nu) F(\nu)\eta(\nu) d\nu}{\int_\nu F(\nu)\eta(\nu) d\nu}, \quad (14)$$

where

$$y(\nu) = \iint_{\text{Beam}} I(\nu, \theta, \phi) B(\nu, \theta, \phi) d\theta d\phi. \quad (15)$$

To derive an estimate of a monochromatic sky surface brightness from the broad-band measurement, it is therefore necessary (i) to have knowledge of the beam response as a function of frequency across the band, (ii) to assume some particular spectral shape for the source emission, and (iii) to assume some particular source spatial distribution. For simplicity, we consider here the case in which both the beam and the source are circularly symmetric, and the source surface brightness profile  $I(\nu, \theta)$  varies with position according to some function  $g(\theta, \theta_0)$  relative to a scale radius  $\theta_0$ , and with frequency according to  $f(\nu, \nu_0)$ , but has the same frequency dependence for all positions:

$$I(\nu, \theta) = I(\nu_0, 0) \cdot f(\nu, \nu_0) \cdot g(\theta, \theta_0). \quad (16)$$

As before, a power law or a modified blackbody could be used for  $f(\nu, \nu_0)$ . A reasonable assumption for the spatial variation could be another power law or a Gaussian function.

The peak surface brightness at frequency  $\nu_0$  is then

$$I(\nu_0, 0) = K_{\text{MonE}}(f, g, \nu_0) \cdot \bar{S}_{\text{Meas}}, \quad (17)$$

where

$$K_{\text{MonE}}(f, g, \nu_0) = \frac{\int_{\nu} F(\nu)\eta(\nu) d\nu}{\int_{\nu} y'(\nu, \theta_0) f(\nu, \nu_0) F(\nu)\eta(\nu) d\nu}, \quad (18)$$

with

$$y'(\nu, \theta_0) = \iint_{\text{Beam}} P(\nu, \theta) g(\theta, \theta_0) 2\pi\theta d\theta, \quad (19)$$

where  $P(\nu, \theta)$  is the circularly symmetric beam profile.

It is important to note that, unlike the point source case,  $K_{\text{MonE}}$  is not dimensionless, but converts from flux density (Jy or Jy beam<sup>-1</sup> for extended sources) to surface brightness (conventionally MJy sr<sup>-1</sup>).

An alternative to the point source calibration scheme described in the previous section would be to assume, as standard, fully extended emission and to derive the sky surface brightness using equation (17). Note that in the case of uniform extended emission filling the beam, where  $g(\theta, \theta_0) = 1$ , the integral over the beam reduces to the frequency-dependent beam solid angle,  $\Omega(\nu)$ , so that

$$\begin{aligned} K_{\text{Uniform}}(f, \nu_0) &\equiv K_{\text{MonE}}(f, g = 1, \nu_0) \\ &= \frac{\int_{\nu} F(\nu)\eta(\nu) d\nu}{\Omega(\nu_0) \int_{\nu} \Omega_{\text{norm}}(\nu, \nu_0) f(\nu, \nu_0) F(\nu)\eta(\nu) d\nu}, \end{aligned} \quad (20)$$

where  $\Omega_{\text{norm}}(\nu, \nu_0) = \Omega(\nu)/\Omega(\nu_0)$  is the beam solid angle normalized to the value at  $\nu_0$ . It is also possible to construct an ‘effective beam solid angle’ for a given source spectrum,  $\Omega_{\text{eff}}(f)$ :

$$\Omega_{\text{eff}}(f) = \frac{\int_{\nu} f(\nu, \nu_0) \Omega(\nu) F(\nu)\eta(\nu) d\nu}{\int_{\nu} F(\nu)\eta(\nu) d\nu}. \quad (21)$$

It may be the case that different processing steps are required for point sources and extended emission. Automatic instrument pipelines must therefore adopt one convention or the other, requiring a post-pipeline correction in the case of a different source type. For example, if the pipeline processing for an extended source is based on the assumption that the observation is of fully extended emission (i.e.  $\theta_0 = \infty$ ) which has a power-law spectrum with  $\alpha = \alpha_0$ , then the extended source pipeline produces a map in which the peak surface brightness is

$$I_{\text{Pipe}}(\alpha_0, \nu_0, \theta = 0) = K_{\text{Uniform}}(\alpha_0, \nu_0) \cdot \bar{S}_{\text{Meas}}(\theta = 0). \quad (22)$$

The conversion from the point source to fully extended source pipelines is relatively straightforward:

$$I_{\text{Pipe}}(\alpha_0, \nu_0, \theta = 0) = \left[ \frac{K_{\text{Uniform}}(\alpha_0, \nu_0)}{K_{\text{MonP}}(\alpha_0, \nu_0)} \right] S_{\text{Pipe}}. \quad (23)$$

The peak surface brightness at frequency  $\nu_0$  for a general extended source can then be derived from the peak of the extended pipeline surface brightness as

$$I(\nu_0, 0) = K_{\text{ColE}}(f, g, \alpha_0, \nu_0) \cdot I_{\text{Pipe}}(\alpha_0, \nu_0, \theta = 0), \quad (24)$$

where

$$\begin{aligned} K_{\text{ColE}}(f, g, \alpha_0, \nu_0) &= \frac{K_{\text{MonE}}(f, g, \nu_0)}{K_{\text{Uniform}}(\alpha_0, \nu_0)} \\ &= \frac{\Omega(\nu_0) \int_{\nu} \Omega_{\text{norm}}(\nu, \nu_0) \left(\frac{\nu}{\nu_0}\right)^{\alpha_0} F(\nu)\eta(\nu) d\nu}{\int_{\nu} y'(\nu, \theta_0) f(\nu, \nu_0) F(\nu)\eta(\nu) d\nu}. \end{aligned} \quad (25)$$

where  $y'(\nu, \theta_0)$  is as defined in equation (19). The variable  $K_{\text{ColE}}$  converts the extended pipeline surface brightness, which assumes a fully extended source with spectral index  $\alpha_0$ , to that for an extended source with brightness profile  $g(\theta, \theta_0)$  and spectrum  $f(\nu, \nu_0)$ .

The monochromatic beam profile and beam solid angle are not normally measured directly, but have to be modelled based on the instrument design and broad-band measurements of a particular source. The broad-band beam profile is usually determined by mapping a point-like source such as a planet. If the source used for the beam mapping has spectral index  $\alpha_p$ , then the resulting measured beam profile is

$$P_{\text{Meas}}(\theta, \alpha_p) = \frac{\int_{\nu} \nu^{\alpha_p} P(\nu, \theta) F(\nu)\eta(\nu) d\nu}{\int_{\nu} \nu^{\alpha_p} F(\nu)\eta(\nu) d\nu}, \quad (26)$$

and the corresponding measured beam solid angle is

$$\Omega_{\text{Meas}}(\alpha_p) = \iint_{\text{Beam}} P_{\text{Meas}}(\theta, \alpha_p) 2\pi\theta d\theta. \quad (27)$$

This method assumes a point-like source, so it may also be necessary to apply a correction for the finite angular size of the calibration target.

#### 4 BEAM PROFILE AND APERTURE EFFICIENCY VARIATION WITHIN THE PASSBAND

The ways in which the beam profile and the aperture efficiency vary across the passband depend on the detector array architecture, in particular on whether the detectors are antenna-coupled (single-moded) or absorber-coupled (multi-moded). Here, we consider two of the most commonly adopted configurations: a feedhorn antenna-coupled system designed to have a horn aperture corresponding to  $2\lambda/D$  (where  $D$  is the telescope aperture) at the band centre in order to give maximum aperture efficiency, and an absorber-coupled system designed to have square pixels of side  $0.5\lambda/D$  at the band centre in order to provide instantaneous Nyquist sampling of the sky image. In both cases, we consider an idealized passband of width given by  $R = \nu/\Delta\nu = \lambda/\Delta\lambda = 3$ , with constant transmission within the band and zero outside.

##### 4.1 Antenna-coupled case

For a diffraction-limited antenna-coupled system (e.g. *Herschel-SPIRE*, *BLAST*), the beam FWHM increases with increasing wavelength within the band due to diffraction at the primary aperture (which gets smaller in relation to the wavelength). In the case of a wavelength-independent illumination of the primary aperture by the detector, this variation would be linear. However, for antenna coupling, it is necessary to take into account the fact that the beam profile of the feed antenna itself broadens with increasing wavelength, so that the aperture illumination profile tends to be less tapered at longer wavelengths. This means that the outer parts of

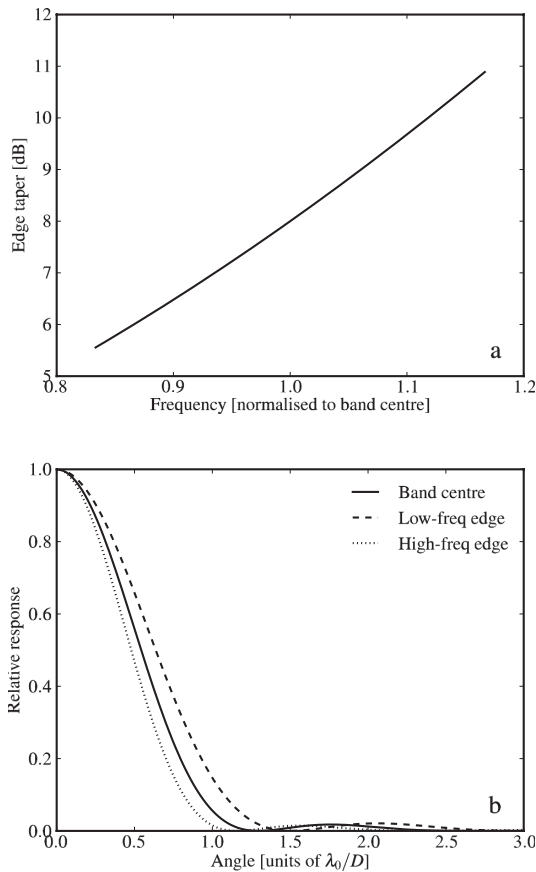


**Figure 1.** (a) Edge taper of the primary illumination versus normalized frequency for the case of a feedhorn producing a Gaussian beam of width inversely proportional to frequency. An edge taper of 8 dB is adopted at the central wavelength of the band, which is taken to have  $R = 3$ . (b) Corresponding beam profiles at the band centre (solid line), low-frequency edge (dashed line) and high-frequency edge (dotted line).

the antenna are more strongly illuminated at longer wavelengths, tending to make the beam narrower and offsetting the effect of diffraction at the primary. The expected variation of beam FWHM with wavelength is therefore slower than linear. To examine this effect, we consider the idealized case of a feed antenna illuminating an unobscured telescope with a Gaussian illumination pattern of width directly proportional to wavelength. The edge taper (relative illumination at the primary edge compared to the on-axis value) is taken to be 8 dB at the centre of a band of width  $R = \nu/\Delta\nu = 3$ .

Fig. 1(a) shows the edge taper of the primary illumination versus normalized frequency. The edge taper varies from 5.9 dB at the low-frequency edge of the band to 11.5 dB at the high-frequency end. The telescope far-field beam profile is calculated as the Fourier transform of the telescope illumination pattern and is shown in Fig. 1(b) for the band centre and edges (with the angular offset in units of  $\lambda_0/D$ , where  $\lambda_0$  is the band centre). The beam FWHM is plotted in Fig. 2(a) as a function of frequency within the band. The variation is well fitted (residuals  $<0.5$  per cent in any part of the band) by a power law:  $\text{FWHM} \propto \nu^\gamma$  with  $\gamma = -0.85$ . The FWHM varies by around  $\pm 17$  per cent across the passband. The normalized beam solid angle,  $\Omega_{\text{norm}}$ , is plotted versus frequency in Fig. 2(b). This variation is well fitted (residuals  $<1$  per cent in any part of the band) by a power law ( $\Omega_{\text{norm}} \propto \nu^\delta$ ) with  $\delta = 1.75$ .

The on-axis aperture efficiency,  $\eta$ , for the case of a smooth-walled conical horn is given in Griffin, Bock & Gear (2002) as a function

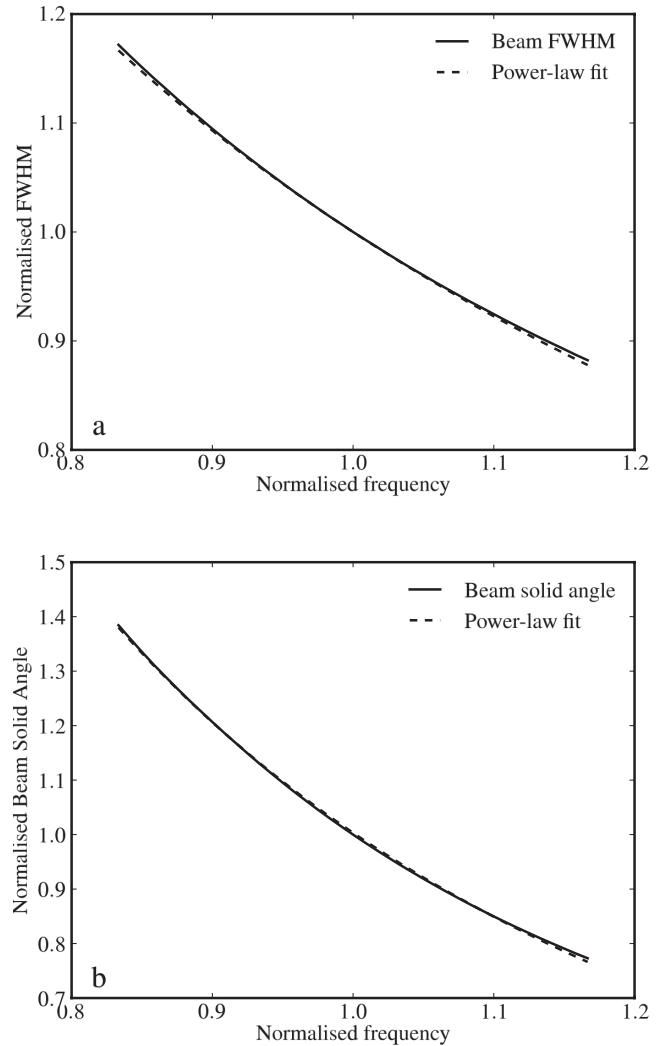


**Figure 2.** (a) Solid line: far-field beam FWHM (normalized to the value at the centre of the band) versus frequency (also normalized to the band centre) for Gaussian beam illumination of the primary with 8 dB edge taper at the band centre. Dashed line: power-law fit where  $\text{FWHM} \propto \nu^\gamma$ , with  $\gamma = -0.85$ . (b) Solid line: beam solid angle (normalized to the value at the centre of the band) versus frequency (also normalized to the band centre) for Gaussian beam illumination of the primary with 8 dB edge taper at the band centre. Dashed line: power-law fit where  $\Omega \propto \nu^\delta$ , with  $\delta = -1.75$ .

of horn aperture diameter in units of  $\lambda/D$ . For a given wavelength, aperture efficiency increases with aperture diameter, reaches a broad maximum of  $\sim 0.75$  at approximately  $2\lambda/D$  and declines for larger aperture size as the feedhorn beam narrows and significantly underilluminates the telescope resulting in a diminution of efficiency. The corresponding aperture efficiency as a function of frequency for a feedhorn which is  $2\lambda/D$  at the centre of a band with  $R = 3$  is shown in Fig. 3. The aperture efficiency has a broad peak and is fairly uniform across the band.

#### 4.2 Absorber-coupled case

The beam solid angle and aperture efficiency in the case of an absorber-coupled detector (e.g. *Herschel*-PACS, SCUBA2) have been computed by convolving the Airy function for diffraction at a circular telescope aperture with a square pixel of side  $0.5\lambda/D$  at

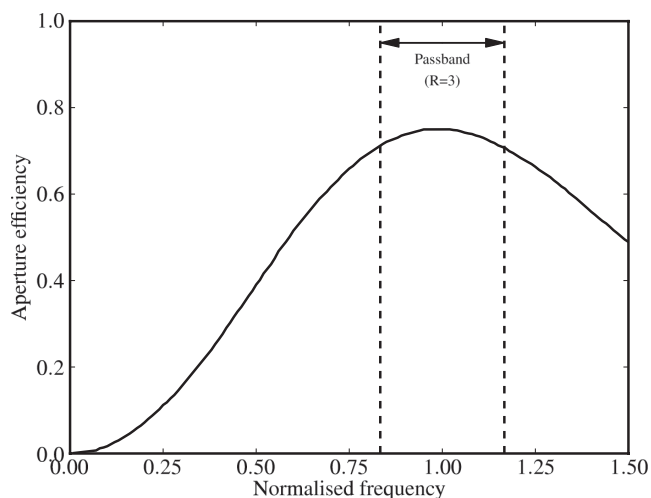


**Figure 3.** Aperture efficiency versus normalized frequency for a conical feedhorn antenna sized to have an entrance aperture of  $2\lambda/D$  at the centre of the passband. The vertical dashed lines indicate a passband with  $R = 3$ .

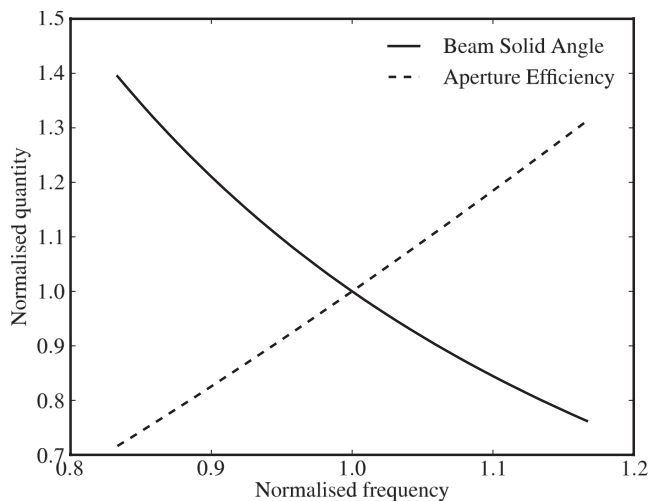


**Figure 4.** Beam solid angle (solid line), aperture efficiency (dashed line) versus frequency within an  $R = 3$  passband for a pixel side of  $0.5\lambda/D$  at the band centre. Both quantities are normalized to those at the band centre, at which frequency the aperture efficiency is 0.178.

the band centre. The results are shown in Fig. 4. Although the aperture efficiency and beam solid angle are both strongly frequency dependent, the product of the two, which determines how the detector couples to fully extended emission, is constant across the band (which must be the case in order to satisfy the requirement that for sky intensity independent of position or frequency, the power per unit frequency intercepted by a pixel must be constant across the band). This is in contrast to the antenna-coupled case described above, where the aperture efficiency does not change much across the band but the beam solid angle is strongly frequency dependent, leading to a much greater variation of coupling efficiency to extended emission over the passband. In the case of fully extended emission with an absorber-coupled detector, it is not necessary to know the frequency dependences of the beam solid angle and aperture efficiency independently. However, for semi-extended emission they must both be taken into account explicitly.

## 5 EXAMPLE: CALIBRATION OF A UNIFORM PASSBAND

As an example we take the case of a passband with  $R = 3$ , an assumed source spectral index  $\alpha_0 = -1$ , and nominal frequency  $\nu_0$  at the band centre, and either a point or fully extended source, and consider the corresponding correction factors as a function of assumed power-law source spectral index, for both the feedhorn and absorber-coupled cases.

The point source colour-correction factor for an assumed power-law spectrum,  $K_{\text{CoIP}}(\alpha, -1, \nu_0)$ , as computed using (11), is shown as a function of source spectral index in Fig. 5(a) for the antenna-coupled case. Also shown in Fig. 5(a) are the colour-correction curves for narrower passbands with  $R = 5$  and  $R = 10$ . The correction factor is seen to be sensitive to the width of the passband. Moving the frequency of the band edges by 1 per cent results in a 1.6 per cent change in the colour-correction factor for a source with spectral index  $\alpha = 3$ . It is found to be much less sensitive to the shape of the passband or the aperture efficiency function: changing the flat passband shape to one with a  $\pm 5$  per cent tilt across the band results in only a 0.5 per cent change in the colour-correction factor. This insensitivity arises from the fact that the SRF integral appears in both the numerator and denominator of e.g. equation (8). The choice of the standard frequency,  $\nu_0$ , also affects the correction significantly, as shown in Fig. 5(b) which illustrates the effect of shifting  $\nu_0$  in either direction by 3 per cent of the bandwidth.

The colour-correction factor for fully extended sources,  $K_{\text{CoIE}}(\alpha, \infty, -1, \nu_0)$ , as given by equation (25), for the feedhorn case with an  $R = 3$  passband, is plotted versus assumed source spectral index in Fig. 5(c). Depending on the source spectral index and the choice of nominal frequency, corrections on the order of 10 per cent may be needed. The correction factors are not very sensitive to the exact value assumed for  $\delta$ , the power-law for the solid angle variation across the band. Changing  $\delta$  by  $\pm 10$  per cent changes the correction factor by less than 1 per cent over the whole range of the plot.

The results for the absorber-coupled case are shown in Fig. 6. The point source colour-correction factor for an assumed power-law spectrum,  $K_{\text{CoIP}}(\alpha, -1, \nu_0)$ , is shown in Fig. 6(a), for a resolution of  $R = 3$  and also for narrower passbands with  $R = 5$  and  $R = 10$ , and a broader band with  $R = 2$  (in the case of an absorber coupled detector, such a broad bandwidth is easily achievable, unlike the feedhorn case). As with the feedhorn-coupled case (Fig. 5a), depending on the source spectral index, colour corrections on the order of 10 per cent can be needed for  $R \sim 3$ , with significantly smaller corrections for narrower bands. For a broader passband, the colour correction can be much larger: up to 20 per cent for  $R \sim 2$ . Changing the nominal frequency at which results are quoted also changes the correction significantly: Fig. 6(b) shows the effect of shifting the nominal frequency in either direction by 3 per cent of the bandwidth. The extended source colour-correction conversion factor,  $K_{\text{CoIE}}(\alpha, \infty, -1, \nu_0)$  is plotted versus assumed source spectral index for the absorber-coupled case with  $R = 3$  in Fig. 6(c).

For either of the two architectures, the exact shapes and positions of the correction curves will depend on the details of the passbands, feed antenna or pixel size, and choice of nominal frequency, and they must be computed explicitly for a given instrument.

## 6 APPLICATION TO THE HERSCHEL-SPIRE PHOTOMETER

The calibration scheme described above has been applied to the *Herschel*-SPIRE camera (Griffin et al. 2010), and full details are

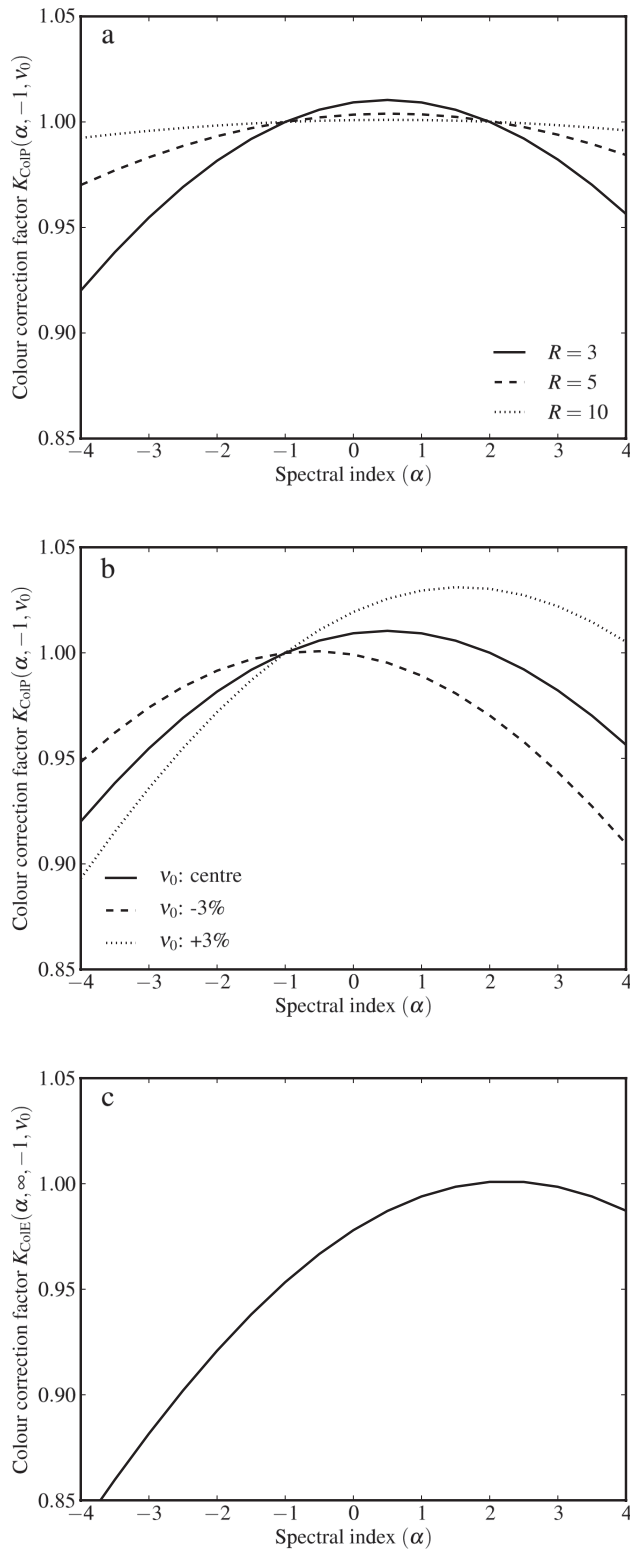


**Figure 5.** (a) Point source colour-correction factor versus power-law source spectral index for a conical feedhorn-coupled system with  $R = 3$  (solid line), 5 (dashed line) and 10 (dotted line) and nominal frequency at the band centre. (b) The same with  $R = 3$  and nominal frequency at the band centre (solid line), shifted by 3 per cent of the bandwidth towards the low-frequency edge (dashed line) and 3 per cent towards the high-frequency edge (dotted line). (c) Extended colour-correction conversion factor (conical feedhorn case;  $R = 3$ ; nominal frequency at band centre; fully extended source) versus assumed source spectral index.

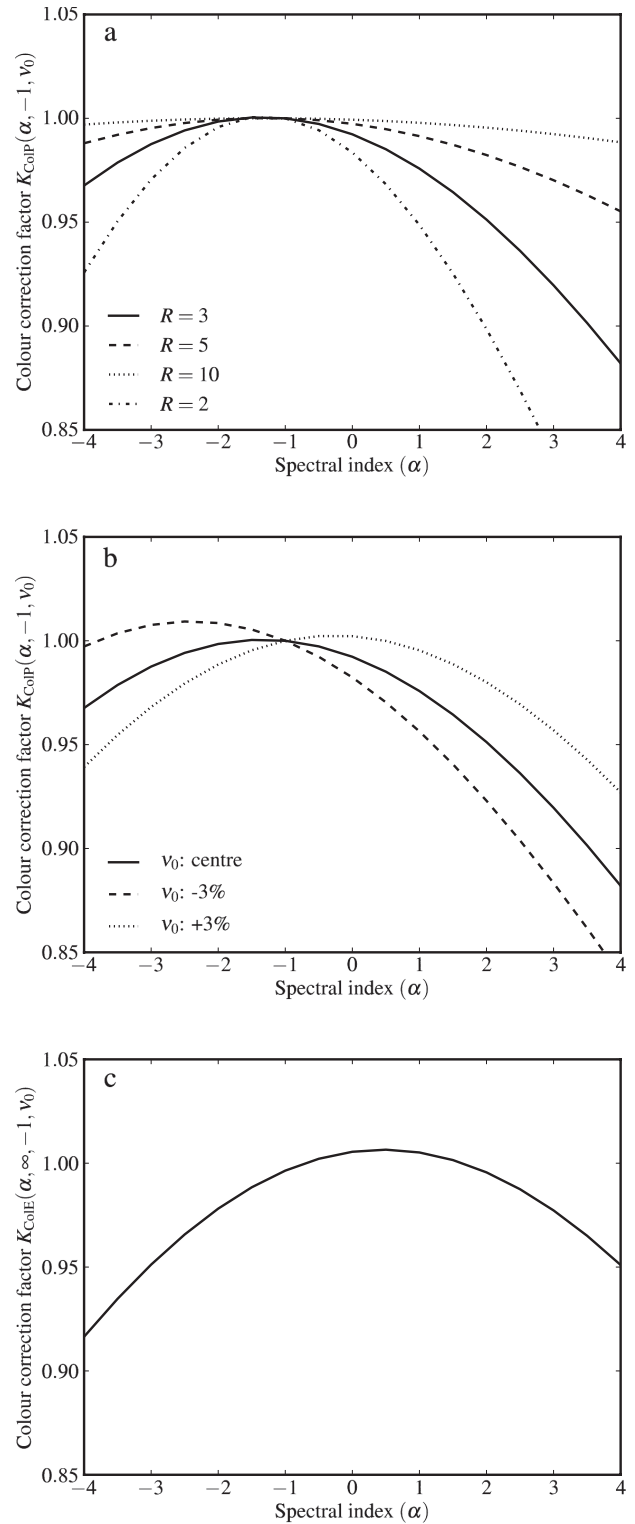


**Figure 6.** (a) Point source colour-correction factor versus power-law source spectral index for an absorber-coupled system ( $\alpha_0 = -1$ ,  $\nu_0$  at band centre, pixel side =  $0.5\lambda/D$  at band centre) with  $R = 3$  (solid line), 5 (dashed line), 10 (dotted line) and 2 (dot-dashed line). (b) The same with  $R = 3$  and nominal frequency at the band centre (solid line), shifted by 3 per cent of the bandwidth towards the low-frequency edge (dashed line) and 3 per cent towards the high-frequency edge (dotted line). (c) Extended colour-correction conversion factor versus assumed source spectral index for an absorber-coupled system ( $R = 3$ ,  $\alpha_0 = -1$ ,  $\nu_0$  at band centre, pixel side =  $0.5\lambda/D$  at band centre; fully extended source).

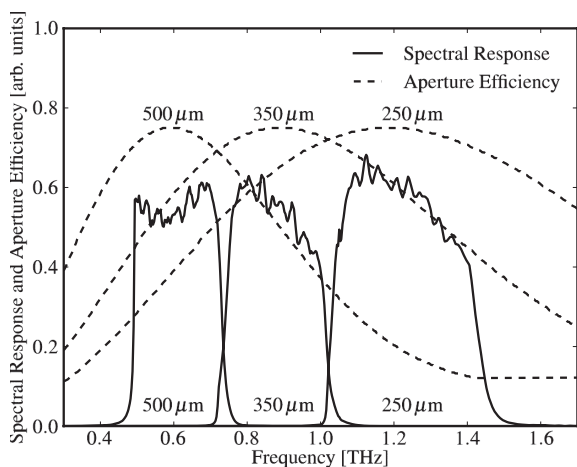


**Figure 7.** SRFs and aperture efficiencies as a function of frequency for the three SPIRE photometer bands. Note that the vertical scale is irrelevant to the computations in this paper as all relevant parameters involve ratios.

given in the SPIRE Observer’s Manual.<sup>1</sup> Here, we summarize the relevant instrument properties and the main results. The SPIRE photometer SRFs are shown in Fig. 7 along with the aperture efficiency functions. These profiles represent the instrument transmission as a function of frequency. The diameters of the feedhorns are sized to correspond to  $2\lambda/D$  at wavelengths of 250, 333 and 500  $\mu\text{m}$ , chosen to provide high on-axis aperture efficiency for all three bands (and to ensure that a significant subset of the detectors in the three arrays overlap on the sky). The SPIRE bands have resolutions of  $R = 2.5\text{--}3.2$ , and so are similar to the  $R = 3$  example discussed in Section 5.

### 6.1 Point source calibration

The SPIRE photometer flux calibration scheme is based on the use of Neptune as the primary calibration source, using the ESA-4 model spectrum of Moreno (2012), and the pipeline is based on the assumption of observations of a point source. The pipeline conversion from detector signal to flux density essentially involves taking the ratio of the source signal to the Neptune signal and multiplying by the Neptune calibration flux density calculated (for the particular time of its observation) using equation (2). Standard wavelengths of 250, 350 and 500  $\mu\text{m}$  are adopted at which the pipeline-produced monochromatic flux densities are derived, using the nominal spectral index  $\alpha_0 = -1$ , and the conversion factor  $K_{\text{MonP}}(-1, \nu_0)$  is applied in the pipeline. Based on the SPIRE SRFs and aperture efficiencies, the values of  $K_{\text{MonP}}(-1, \nu_0)$ , given by equation (9), are (1.0102, 1.0095, 1.0056) for the (250, 350, 500)  $\mu\text{m}$  bands. These numbers are not particularly sensitive to the exact shape of the SRF or the aperture efficiency function – for instance, assuming a flat SRF and constant aperture efficiency across the band would give values of (1.0121, 1.0132, 1.0065).

The SPIRE point source colour-correction factors for an assumed power-law spectrum,  $K_{\text{CoIP}}(\alpha, -1, \nu_0)$ , as computed using equation (11), is shown in Fig. 8(a). Typical dust sources have  $\alpha$  in the range 1–3 in the SPIRE range, requiring colour-correction factors of a few per cent – 10 per cent. For a  $\nu^3$  source, the colour-correction factors are (0.9121, 0.9161, 0.9005) for the (250, 350, 500)  $\mu\text{m}$

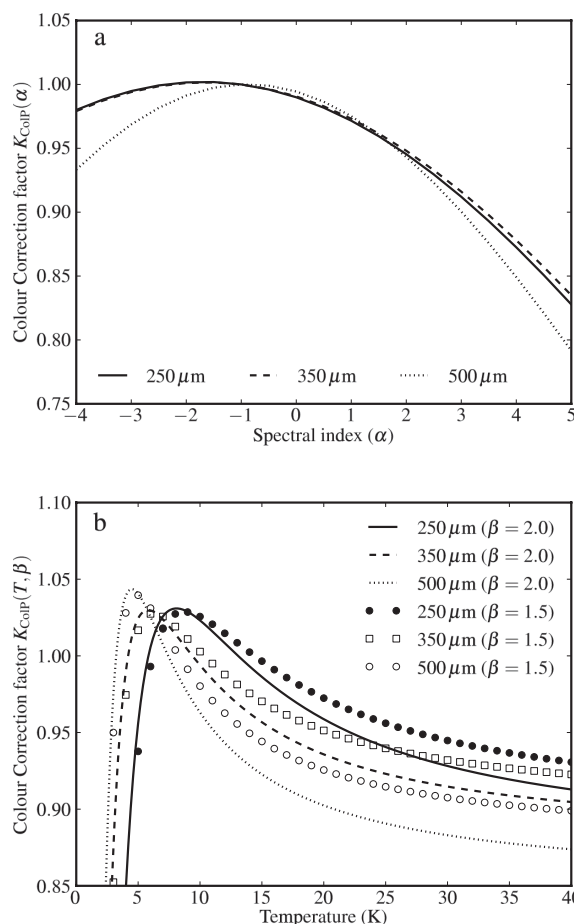


**Figure 8.** SPIRE point source colour-correction parameter assuming (a) a power-law source spectrum, showing  $K_{\text{CoIP}}(\alpha, -1, \nu_0)$  versus assumed source spectral index, and (b) a modified blackbody spectrum, showing  $K_{\text{CoIP}}(T, \beta, -1, \nu_0)$ , versus source temperature for  $\beta = 2$  (lines) and 1.5 (symbols).

bands. The approximation to a power law is reasonably accurate for a modified blackbody across a single SPIRE passband for all but the lowest dust temperatures.

Fig. 8(b) shows the modified blackbody colour-correction factors as a function of temperature up to 40 K for two commonly adopted values of modified blackbody emissivity index:  $\beta = 1.5$  and 2. The necessary correction varies significantly with source temperature. For temperatures in the higher part of the range and  $\beta = 2$ , the correction factors are comparable to the power-law case with  $\alpha = 4$ . The lower value of  $\beta$  results in smaller colour corrections, as expected for a less steep spectrum.

As shown in Section 2, it is the value of  $K_{\text{MonP}}(\alpha, \nu_0)$  which converts the measured SRF-weighted flux density to the final estimate of the source monochromatic flux density. It is not particularly sensitive to the assumed shape of the SRF or aperture efficiency functions. For instance, for a  $\nu^3$  source, using  $F(\nu)$  and  $\eta(\nu)$  as above gives overall factors of  $K_{\text{MonP}}(3, \nu_0) = (0.921, 0.925, 0.905)$  at (250, 350, 500)  $\mu\text{m}$ . Assuming instead a top-hat SRF and constant aperture efficiency across the band would give values of (0.917, 0.918, 0.907). The exact shapes of the SRFs for individual pixels vary across the detector arrays, with the dominant effect being the movement of the band edges by  $\sim 1$  per cent rms. Using the measured variations from the pre-launch SRF characterization measurements, the spread in colour-correction parameters is 1–2 per cent. This is in agreement

<sup>1</sup> The SPIRE Observer’s Manual is available at [http://herschel.esac.esa.int/Docs/SPIRE/pdf/spire\\_om.pdf](http://herschel.esac.esa.int/Docs/SPIRE/pdf/spire_om.pdf)

for the general case discussed in Section 5, and well within the SPIRE error budget. The effect is larger for sources with extreme spectral indices, and is also larger for the broader 500  $\mu\text{m}$  band.

## 6.2 Extended source calibration

The SPIRE beams used for extended source calibration are derived from the fine-grid scan maps of Neptune (Bendo et al., in preparation) shown at 1 arcsec pixel resolution in Fig. 9. To produce these maps, the telescope was scanned across Neptune such that all bolometers contribute equally to the map – resulting in an average over all the detectors in a given array. Diffuse background emission and point sources have been removed from these maps.

### 6.2.1 Beam profiles

Azimuthally averaged profiles from the measured maps are shown in Fig. 10 and exhibit high signal-to-noise ratio down to response levels  $\sim 10^{-5}$  and out to a radius of  $\sim 250$  arcsec. Lower level structure, between  $10^{-5}$  and  $10^{-6}$ , due to the diffraction spikes produced by the secondary support structure, is evident in the 300–500 arcsec range with the same basic structure for all three bands. The solid angles of these measured band-averaged beams (computed out to a radius of 700 arcsec) are  $\Omega_{\text{Meas}} = (450, 795, 1665) \text{ arcsec}^2$  for (250, 350, 500)  $\mu\text{m}$ , with uncertainties of 4 per cent arising from uncertainties in the baseline level. This uncertainty is expected to be reduced in the future by subtracting a shadow map of the same field without Neptune.

In order to create a monochromatic model for the SPIRE beams, each azimuthally averaged beam has been split into two sections: an inner section representing diffraction from the primary aperture,  $P_{\text{inner}}(\theta)$ , which will be scaled radially with frequency, and an outer section which does not scale with frequency ( $P_{\text{outer}}(\theta)$ ). The beam profile features in this outer section do not change significantly in angular position in the measurements of the three bands (though they are generally broader at longer wavelengths). This suggests that they are due to fixed objects on the spacecraft, such as the secondary mirror support, and that they do not vary with frequency within the bands. To derive a function for the beam profile versus frequency across the band, we assume that the measured broad-band beam corresponds to the monochromatic beam at some frequency,  $\nu_{\text{eff}}$ , which can be computed as shown below. The beam profile at frequency  $\nu$  within the band,  $P_{\text{mod}}(\theta, \nu, \nu_{\text{eff}})$ , is calculated by allowing the width of the inner component,  $P_{\text{inner}}(\theta)$ , to be scaled as  $(\nu/\nu_{\text{eff}})^\gamma$  (where  $\gamma = -0.85$ , as shown in Section 4.1), while that of the outer component ( $P_{\text{outer}}(\theta)$ ) is kept constant with frequency:

$$P_{\text{mod}}(\theta, \nu, \nu_{\text{eff}}) = \max \begin{cases} P_{\text{inner}}(\theta)/(\nu/\nu_{\text{eff}})^\gamma \\ P_{\text{outer}}(\theta) \end{cases}. \quad (28)$$

Adopting  $P_{\text{mod}}(\theta, \nu, \nu_{\text{eff}})$  as the monochromatic beam, the corresponding predicted broad-band beam when observing Neptune (spectral index  $\alpha_{\text{Nep}}$ ) is

$$P_{\text{Pred}}(\theta, \alpha_{\text{Nep}}, \nu_{\text{eff}}) = \frac{\int_{\nu} \nu^{\alpha_{\text{Nep}}} F(\nu) P_{\text{mod}}(\theta, \nu, \nu_{\text{eff}}) d\nu}{\int_{\nu} \nu^{\alpha_{\text{Nep}}} F(\nu) d\nu}, \quad (29)$$

with a corresponding predicted beam solid angle given by

$$\Omega_{\text{Pred}}(\alpha_{\text{Nep}}, \nu_{\text{eff}}) = \iint_{\text{Beam}} P_{\text{Pred}}(\theta, \alpha_{\text{Nep}}, \nu_{\text{eff}}) 2\pi\theta d\theta. \quad (30)$$

The optimum value of  $\nu_{\text{eff}}$  is the value that results in this predicted solid angle being equal to the measured value,  $\Omega_{\text{Meas}}$ . For all three

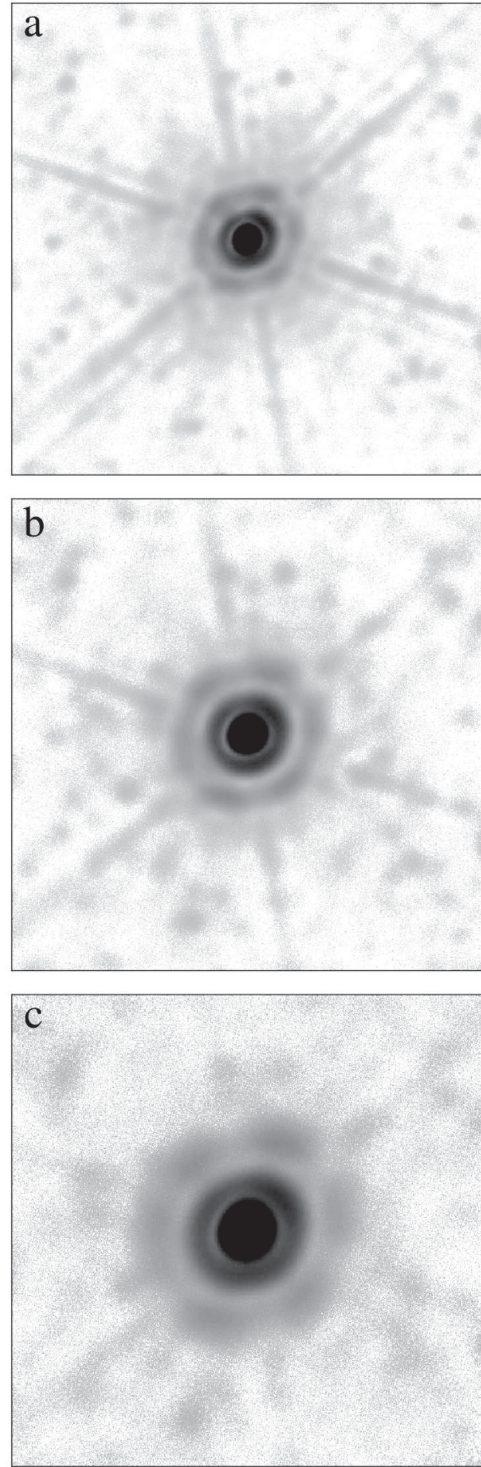


**Figure 9.** Broadband SPIRE beam maps at (a) 250  $\mu\text{m}$ , (b) 350  $\mu\text{m}$  and (c) 500  $\mu\text{m}$ . All plots have the same linear spatial scale (a width of 10 arcmin) and logarithmic colour scale (covering a range of  $[10^{-5}:1]$  relative to the peak value). The beam maps are of Neptune, which has a spectral index of  $\alpha_{\text{Nep}} = (1.29, 1.42, 1.47)$  in the SPIRE (250, 350, 500)  $\mu\text{m}$  bands. The maps show the main beam, which is broader at longer wavelengths, the six symmetric diffraction spikes due to the secondary mirror support structure. The signal-to-noise ratio is higher at shorter wavelengths.

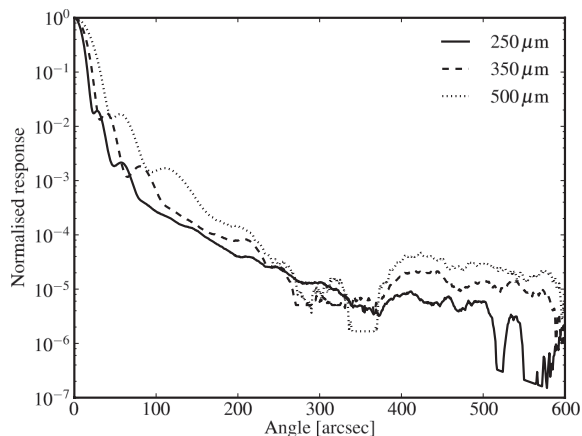


**Figure 10.** Azimuthally averaged measured broad-band beam profiles for the three SPIRE bands.

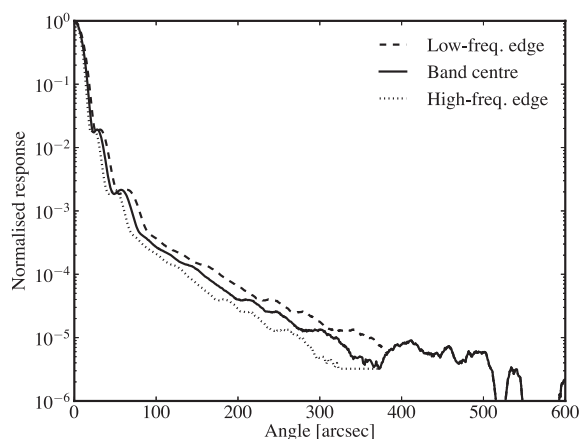


**Figure 11.** SPIRE monochromatic beam profile at frequency  $\nu_{\text{eff}}$  for the 250  $\mu\text{m}$  band and at the two band edges.

bands, frequency  $\nu_{\text{eff}}$  turns out to be around 2 per cent different from the nominal band frequencies, with  $\nu_{\text{eff}} = (1.0188, 1.0173, 1.022)\nu_0$  for the (250, 350, 500)  $\mu\text{m}$  bands. The corresponding monochromatic beam profile for the 250  $\mu\text{m}$  band is shown in Fig. 11 for frequency  $\nu_{\text{eff}}$ , and for the two edges of the band. The predicted and measured broad-band beam profiles are in good agreement, as illustrated for the 250  $\mu\text{m}$  band in Fig. 12.

Once the value of  $\nu_{\text{eff}}$  is fixed, the modelled beam profile can be used with equation (21) to produce an effective beam solid angle for a given source spectrum, as plotted in Fig. 13 for power law and modified blackbody spectra.

### 6.2.2 Comparison with theoretical beam model

An optical model of the telescope and instrument (Sibthorpe et al. 2003), covering a radius out to 300 arcsec, produces FWHM beam widths at  $\nu_{\text{eff}}$  of (17.4, 24.5, 35.0) arcsec, in good agreement with the measured values of (17.6, 23.9, 35.2) arcsec at (250, 350, 500)  $\mu\text{m}$  as given in the SPIRE Observer's Manual. The detailed sidelobe structure and diffraction spikes are well reproduced by the model broad-band beams, but the modelled solid angles are 7–9 per cent smaller than the measured solid angles. This may reflect contributions by additional stray light and diffractive effects not explicitly accounted for in the model.

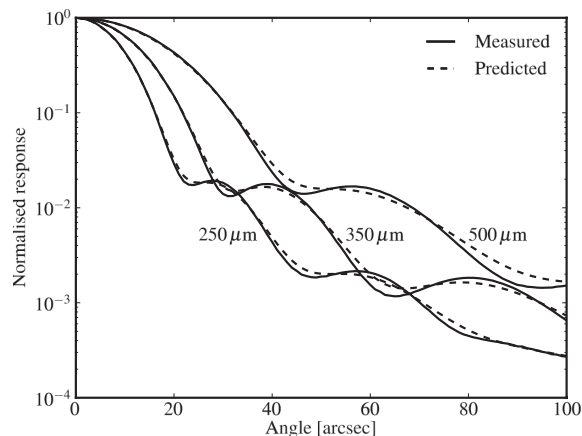


**Figure 12.** Measured (solid line) and predicted (dotted line) broad-band beam profiles for the three SPIRE bands. The beam solid angles are equal by definition.

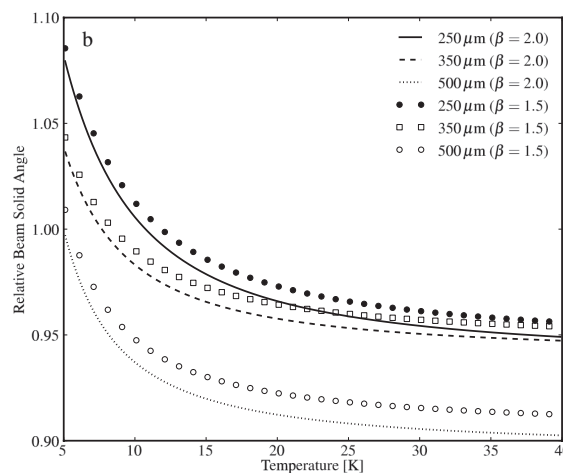
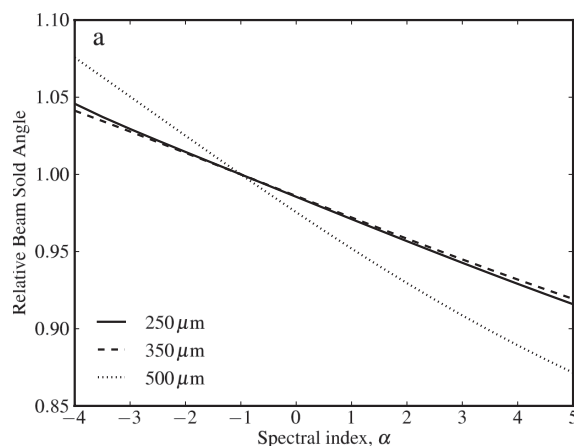


**Figure 13.** Effective beam solid angle, based on the modelled beam profiles for the three SPIRE bands, for sources with (a) a range of spectral indices and (b) a range of temperatures for two values of  $\beta$ .

### 6.2.3 Results for a fully extended source

The factors for converting from the point source pipeline to the extended source pipeline for SPIRE are (90.681, 51.432, 23.908)  $\text{MJy sr}^{-1} \text{Jy}^{-1}$  for the (250, 350, 500)  $\mu\text{m}$  bands. The colour-correction factors for fully extended sources,  $K_{\text{ColE}}(f, \infty, -1, \nu_0)$ ,

for converting the standard SPIRE extended pipeline surface brightness to the value for a fully extended source of a given spectrum, are plotted in Fig. 14(a) (tabulations of this and the other results shown below for SPIRE are given in the SPIRE Observer’s Manual). These results are not sensitive to a small change in the adopted value of  $\gamma$ , the power-law index of the frequency scaling of the beam profile. For a  $\nu^3$  source, using  $\gamma = 0.75$  or  $0.95$  instead of  $0.85$  results in  $K_{\text{CoIE}}(3, \infty, -1, \nu_0)$  changing by less than 0.1 per cent for all three bands. However, assuming that the beam profile is independent of frequency ( $\gamma = 0$ ) results in values which are up to 10 per cent different for the three bands.

$K_{\text{CoIE}}(T, \beta, \infty, -1, \nu_0)$ , the correction factor for an assumed modified black body spectrum, is shown as a function of modified blackbody temperature in Fig. 14(b) for  $\beta = 1.5$  and  $2$ . The dependence on  $\beta$  is small, and the dependence on  $T$  is also small for temperatures above  $\sim 5$  K for the  $500 \mu\text{m}$  band and  $\sim 10$  K for the  $250 \mu\text{m}$  band.

An earlier version of the SPIRE calibration scheme (Swinyard et al. (2010) and SPIRE Observer’s Manual v2.4 and earlier) accounted for the variation of beam size across the band by weighting

the SRF by the square of the wavelength (equivalent to  $\gamma = 1$  and  $\delta = 2$ ), producing a larger throughput at the longer wavelength end of the band. Different colour-correction factors were derived and quoted for the case of point and extended sources, and the conversion from flux density to surface brightness was carried out by dividing by the broad-band beam area as measured on Neptune. Compared to the new method presented here, this earlier method produced surface brightness values which are higher by approximately (7, 7, 12) per cent at (250, 350, 500)  $\mu\text{m}$  for a  $\nu^3$  source. We note that these systematic errors were within the  $\pm 15$  per cent quoted uncertainties.

It is also interesting to compare the results obtained for a fully extended source using the new method and by simply dividing the pipeline output by the measured broad-band beam area. For a source of spectral index  $\alpha$ , this produces an estimate of the sky surface brightness that departs from the true value by a factor of  $G(\alpha)$  given by

$$G(\alpha) = \frac{K_{\text{MonP}}(\alpha, \nu_0)}{K_{\text{Uniform}}(\alpha, \nu_0)\Omega_{\text{Meas}}}. \quad (31)$$

The effect is greater for sources with spectra that are more different from that of Neptune. For a  $\nu^2$  source,  $G(2) = (0.991, 0.990, 0.988)$  and for  $\nu^3$ ,  $G(3) = (0.976, 0.976, 0.966)$ . The sky intensity, which depends on the source spectral index, is thus underestimated by a small extent, and can be up to  $\sim 3$  per cent at  $500 \mu\text{m}$  for a  $\nu^3$  source.

#### 6.2.4 Results for a partially extended Gaussian source

A partially extended source lies between the point-like and fully extended sources. The conversion factor from the extended pipeline peak surface brightness (which applies to a fully extended source, as adopted for the SPIRE extended source pipeline) to the peak surface brightness for a partially extended source,  $K_{\text{CoIE}}(\alpha, \theta_0, -1, \nu_0)$  is plotted versus the source FWHM in Fig. 15 for the case of  $\alpha = 3$  (a typical value for a cold dust source observed by SPIRE). For large source widths (i.e.  $\theta_0 \rightarrow \infty$ ), it converges on the colour-correction parameters plotted in Fig. 14(a), which are close to unity,

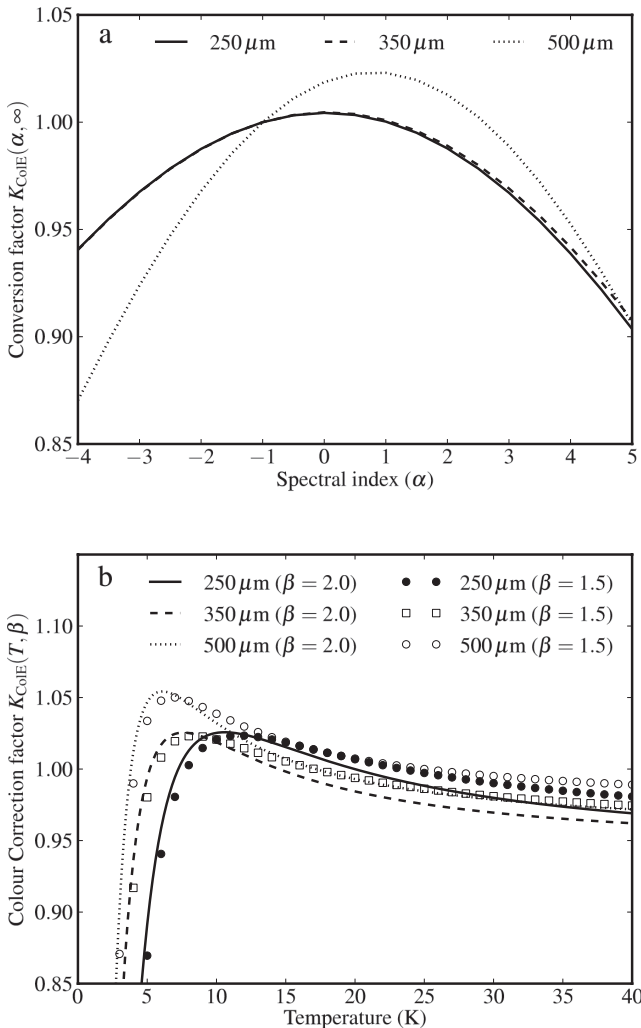


**Figure 14.** The colour-correction factor for a fully extended source, assuming (a) a power-law source spectrum and (b) a modified blackbody source spectrum with  $\beta = 2$  (lines) and  $1.5$  (symbols).

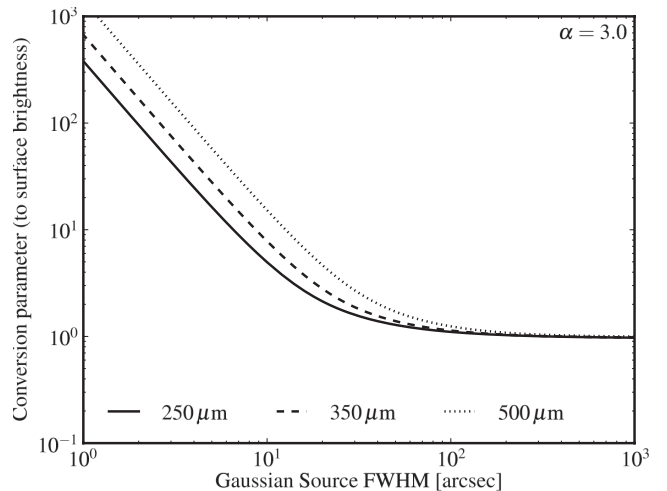


**Figure 15.** Conversion factor from the surface brightness produced by the extended source pipeline to the peak surface brightness of a partially extended source, plotted against the source FWHM, for a source with  $\alpha = 3$ .

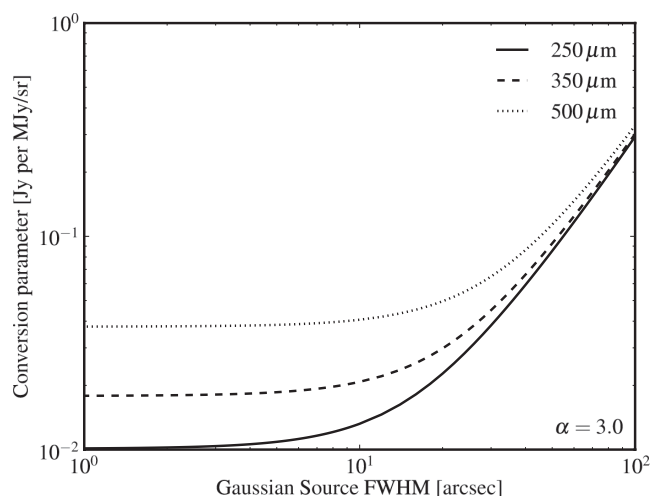


**Figure 16.** Conversion factor from the surface brightness produced by the extended source pipeline to the total flux density of a partially extended Gaussian source, plotted against the source FWHM, for the case of  $\alpha = 3$ .

since the peak value tends towards the surface brightness of a fully extended source. For small sources, this conversion also includes the compensation for the fact that the flux is from a smaller solid angle, defined by the combination of the source size and the effective beam, and so the peak value of the true source surface brightness must increase.

The total flux density of a partly extended source can be calculated by multiplying the peak surface brightness by the effective source area. The corresponding conversion factor between the peak pipeline surface brightness and the total integrated flux density of the source is plotted as a function of source FWHM in Fig. 16. For very small sources (i.e.  $\theta_0 \rightarrow 0$ ), this converges on a value that returns the colour-corrected point source flux. For large sources the total flux density increases with the source area.

## 7 CONCLUSIONS

We have developed a methodology for flux calibration of FIR–submillimetre observations made with broad-band instruments, using either antenna-coupled or absorber-coupled detectors. It takes into account the variation of beam width and aperture efficiency across the photometric band. It can accommodate arbitrary source SEDs and, in the case of extended emission, arbitrary source surface brightness profiles. Accurate knowledge of the instrument properties and of the beam profile is needed to ensure that extended emission can be calibrated with respect to a point source standard.

Application of this scheme to the case of the *Herschel*-SPIRE photometer produces results which are a few per cent higher than those obtained by ignoring the fact that the beam profile varies across the passband. Although not large, these systematic effects are comparable to the absolute uncertainties of the primary calibrator, and so need to be understood and eliminated from the overall error budget.

Similar considerations will apply to other broad-band photometric instruments (space borne in the submillimetre region or ground based at longer wavelengths). Additional practical aspects of SPIRE flux calibration are covered in a companion paper Bendo et al. (in preparation) and in the SPIRE Observer’s Manual.

## ACKNOWLEDGEMENTS

*Herschel* is an ESA space observatory with science instruments provided by European-led Principal Investigator consortia and with important participation from NASA.

SPIRE has been developed by a consortium of institutes led by Cardiff Univ. (UK) and including: Univ. Lethbridge (Canada); NAOC (China); CEA, LAM (France); IFSI, Univ. Padua (Italy); IAC (Spain); Stockholm Observatory (Sweden); Imperial College London, RAL, UCL-MSSL, UKATC, Univ. Sussex (UK); and Caltech, JPL, NHSC, Univ. Colorado (USA). This development has been supported by national funding agencies: CSA (Canada); NAOC (China); CEA, CNES, CNRS (France); ASI (Italy); MCINN (Spain); SNSB (Sweden); STFC, UKSA (UK); and NASA (USA).

This research made use of `APLPHY`, an open-source plotting package for PYTHON hosted at <http://aplyphy.github.com>

## REFERENCES

- Ade P. A. R. et al., 2010, *A&A*, 520, A11  
 Armitage-Caplan C. et al., 2011, preprint (arXiv:1102.2181)  
 Beichman C. A., Neugebauer G., Habing H. J., Clegg P. E., Chester T. E., 1988, *Infrared Astronomical Satellite (IRAS) Catalogs and Atlases*, Vol. 1: Explanatory Supplement. GPO, Washington, DC  
 Bendo G. et al., 2013, *MNRAS*, 433, 3062  
 Bernard J.-P. et al., 2010, in 38th COSPAR Scientific Assembly, Vol. 38, p. 4075  
 Cesarsky C. J. et al., 1996, *A&A*, 315, L32  
 Glenn J. et al., 2003, in Phillips T. G., Zmuidzinas J., eds, *Proc. SPIE*, Vol. 4855, *Millimeter and Submillimeter Detectors for Astronomy*. SPIE, Bellingham, p. 30  
 Griffin M. J., Orton G. S., 1993, *Icarus*, 105, 537  
 Griffin M. J., Bock J. J., Gear W. K., 2002, *App. Opt.*, 41, 6543  
 Griffin M. J. et al., 2010, *A&A*, 518, L3  
 Hauser M. G., Kelsall T., Leisawitz D., Weiland J., 1998, *COBE Diffuse Infrared Background Experiment (DIRBE) Explanatory Supplement*, version 2.3. NASA, Greenbelt  
 Holland W. S. et al., 1999, *MNRAS*, 303, 659  
 Holland W. et al., 2006, *Proc. SPIE*, 6275  
 Lemke D. et al., 1996, *A&A*, 315, L64  
 Moreno R., 1998, PhD thesis, Univ. Paris  
 Moreno R., 2012, Technical Report, Neptune and Uranus Planetary Brightness Temperature Tabulation. ESA Herschel Science Centre, available at: <ftp://ftp.sciops.esa.int/pub/hsc-calibration/PlanetaryModels/ESA4/>  
 Pascale E. et al., 2008, *ApJ*, 681, 400  
 Poglitsch A. et al., 2010, *A&A*, 518, L2  
 Reichborn-Kjennerud B. et al., 2010, *Proc. SPIE*, 7741  
 Ruhl J. et al., 2004, in Bradford C. M. et al., eds, *Proc. SPIE*, Vol. 5498, *Millimeter and Submillimeter Detectors for Astronomy II*. SPIE, Bellingham, p. 11  
 Runyan M. C. et al., 2003, *ApJS*, 149, 265  
 Sibthorpe B., Ferlet M., Bendo G., Papageorgiou A., Technical Report, SPIRE ICC, 2011, *Spire Beam Model Release Note*, Version 1.1. ESA Herschel Science Centre, available at: [http://herschel.esac.esa.int/twiki/pub/Public/SpireCalibrationWeb/beam\\_release\\_note\\_v1-1.pdf](http://herschel.esac.esa.int/twiki/pub/Public/SpireCalibrationWeb/beam_release_note_v1-1.pdf)  
 Siringo G. et al., 2009, *A&A*, 497, 945  
 Siringo G. et al., 2010, *The Messenger*, 139, 20  
 Stansberry J. A. et al., 2007, *PASP*, 119, 1038  
 Swinyard B. M. et al., 2010, *A&A*, 518, L4  
 Ulich B. L., Haas R. W., 1976, *ApJS*, 30, 247

## APPENDIX A

A list of symbols used in the paper is given in Table A1.

**Table A1.** List of symbols.

Symbol	Definition
$\mathcal{B}(\nu, T)$	Planck function for temperature, $T$ , and frequency, $\nu$
$B(\nu, \theta, \phi)$	The beam response as a function of position $(\theta, \phi)$ and frequency, $\nu$
$F(\nu)$	Spectral response function (SRF) of a photometric band in terms of frequency, $\nu$
$f(\nu, \nu_0)$	Source spectrum normalized to the flux density at frequency $\nu_0$
$g(\theta, \theta_0)$	Radial intensity profile, as a function of radial offset angle $\theta$ , of a source with a width characterized by parameter $\theta_0$
$G(\alpha)$	Factor by which a naïve approach to extended source calibration results is an incorrect estimate of the sky surface brightness
$I_{\text{Pipe}}(\alpha_0, \nu_0)$	Monochromatic peak surface brightness of a fully extended source produced by the extended source pipeline, assuming a spectral index $\alpha_0$ .
$I(\nu, \theta)$	Radial source surface brightness profile as a function of frequency $\nu$ and radial offset angle $\theta$ .
$I(\nu, \theta, \phi)$	Radial source surface brightness as a function of frequency $\nu$ and angular position $(\theta, \phi)$ .
$K_{\text{Beam}}(\theta_P, \theta_{\text{Beam}})$	Beam-correction factor for a Gaussian main beam coupling to a uniform disc source
$K_{\text{ColE}}(f, g, \alpha_0, \nu_0)$	Factor to convert the monochromatic pipeline extended source surface brightness, $I_{\text{Pipe}}(\nu_0)$ , to the true peak surface brightness of a source with spectrum $f(\nu, \nu_0)$ and spatial variation $g(\theta, \theta_0)$ .
$K_{\text{ColP}}(f, \alpha_0, \nu_0)$	Colour-correction factor to convert the monochromatic pipeline point source flux density at nominal frequency $\nu_0$ , $S_{\text{Pipe}}(\nu_0)$ , to that corresponding to a different assumed source spectrum $f(\nu, \nu_0)$ .
$K_{\text{MonE}}(f, g, \nu_0, \theta_0)$	Factor to convert SRF-weighted flux density, $\bar{S}_{\text{Meas}}$ , to monochromatic surface brightness, $I(\nu)$ , at frequency $\nu$ for an extended source with spectrum $f(\nu, \nu_0)$ and spatial variation $g(\theta, \theta_0)$ .
$K_{\text{MonP}}(f, \nu_0)$	Factor to convert SRF-weighted flux density, $\bar{S}_{\text{Meas}}$ to monochromatic flux density, $S(\nu_0)$ , at frequency $\nu_0$ for a point source with a spectrum given by $f(\nu, \nu_0)$ .
$K_{\text{Uniform}}(f, \nu_0)$	The conversion parameter for a fully extended source, i.e. $K_{\text{MonE}}(f, g, \alpha_0, \nu_0)$ with $\theta_0 = \infty$ and therefore $g(\theta, \theta_0) \equiv 1$
$P(\nu, \theta)$	Normalized, azimuthally averaged beam profile as a function of radial offset angle $\theta$ and frequency $\nu$
$P(\nu, \theta, \phi)$	Normalized beam response as a function of orthogonal offset angles $\theta$ and $\phi$ , and frequency $\nu$
$P_{\text{inner}}(\theta), P_{\text{outer}}(\theta)$	Inner and outer portions of the monochromatic beam profile. The inner portion is scaled with frequency, while the outer portion is not.
$P_{\text{Meas}}(\theta, \alpha)$	Broad-band beam profile measured on a source of spectral index $\alpha$
$P_{\text{mod}}(\theta, \nu, \nu_{\text{eff}})$	Modelled monochromatic beam profile at frequency $\nu$ , assuming the measured beam is equivalent to the monochromatic beam at frequency $\nu_{\text{eff}}$
$P_{\text{Pred}}(\theta, \alpha, \nu_{\text{eff}})$	Predicted broad-band beam profile for a source spectral index $\alpha$ and effective frequency $\nu_{\text{eff}}$
$R$	Passband width relative to the central frequency
$S(\nu)$	Source flux density at frequency $\nu$
$\bar{S}_{\text{C}}$	SRF-weighted flux density for a calibration source
$\bar{S}_{\text{Meas}}$	SRF-weighted flux density for an observed source
$S_{\text{Pipe}}(\alpha_0, \nu_0)$	Monochromatic flux density at frequency $\nu_0$ produced by a pipeline that assumes point source calibration and a source spectral index of $\alpha_0$
$T$	Blackbody or modified blackbody temperature
$y(\nu)$	Monochromatic flux density at frequency $\nu$ for an extended source with surface brightness $I(\nu, \theta, \nu)$ , integrated over a monochromatic beam with response $B(\nu, \theta, \phi)$
$y'(\nu, \theta_0)$	Normalized monochromatic flux density at frequency $\nu$ for an extended source with radial intensity profile $g(\theta, \theta_0)$ , integrated over a monochromatic beam with radial profile $P(\nu, \theta)$
$\alpha$	Astronomical source power-law spectral index
$\alpha_0$	Nominal source spectral index for which SPIRE flux densities are quoted
$\alpha_{\text{Nep}}$	Spectral index adopted for Neptune when used as a SPIRE photometric calibrator
$\beta$	Modified blackbody emissivity index such that emissivity $\propto \nu^\beta$
$\gamma$	Power-law index for adopted variation of main beam FWHM with frequency
$\delta$	Power-law index for adopted variation of beam solid angle with frequency
$\eta(\nu)$	Aperture efficiency (total power coupled to detector from an on-axis source) as a function of frequency, $\nu$
$\theta$	Radial offset angle from the centre of the beam
$\theta_0$	Width parameter of a source with a circularly symmetric intensity profile
$\theta_{\text{Beam}}$	Beam FWHM used for calibration
$\theta_P$	Angular radius of observed planetary disc used as a calibrator
$\lambda, \nu$	Radiation wavelength and frequency
$\Delta\lambda, \Delta\nu$	Bandwidth of photometer passband in terms of wavelength and frequency
$\nu_0$	Nominal frequency at which monochromatic source flux density is to be quoted
$\nu_{\text{eff}}$	Effective frequency at which the monochromatic beam profile is assumed to be equal to the measured beam profile, and constrained such that $\Omega_{\text{Pred}}$ is equal to $\Omega_{\text{Meas}}$
$\phi$	Azimuthal offset angle relative to the beam centre, used in non-circularly symmetric cases
$\Omega(\nu)$	Monochromatic beam solid angle at frequency $\nu$
$\Omega_{\text{eff}}(f)$	Effective beam solid angle for observations of a source with spectrum $f(\nu, \nu_0)$
$\Omega_{\text{Meas}}(\alpha)$	Broad-band beam solid angle as measured on a point source of spectral index $\alpha$
$\Omega_{\text{norm}}(\nu, \nu_0)$	Monochromatic beam solid angle at frequency $\nu$ normalized to the value at $\nu_0$
$\Omega_{\text{Pred}}(\alpha, \nu_{\text{eff}})$	Predicted beam solid angle for a source with spectral index $\alpha$ , assuming an effective frequency $\nu_{\text{eff}}$